metals

Article

Investigation of Residual Stress Variation in Sequential Butt Welding and Pocket Material Removal Machining Processes Utilizing Pre-Stress Method: A 3D Simulation Approach

Isik Cetintav [1,*], **Yilmaz Can** [1] and **Nihat Akkus** [2]

[1] Department of Mechanical Engineering, Faculty of Engineering, Trakya University, 22030 Edirne, Turkey; ycan@trakya.edu.tr
[2] Department of Mechatronics Engineering, Gedik University, 34953 Istanbul, Turkey; nihat.akkus@gedik.edu.tr
* Correspondence: isikcetintav@trakya.edu.tr

Abstract: This study investigates the residual stresses arising from welding and machining processes, recognizing their adverse implications in manufacturing. Employing experimental analysis and simulation techniques, the research scrutinizes residual stress alterations resulting from sequential butt welding and subsequent machining. Utilizing MSC Marc Mentat software(version 2016), three-dimensional models are developed to simulate these processes. The finite element model from welding simulation seamlessly integrates into cutting simulations via the pre-state option. The experimental procedures involve 100 × 100 × 10 mm AISI 304 steel plates subjected to sequential welding and machining, with residual stresses measured at each stage. A comparative analysis between experimental and simulation results elucidates variations in residual stresses induced by sequential processes. The study focuses on examining the initial stress state post-welding and numerically assessing stress modifications due to milling. The results suggest minimal material removal insignificantly affects stress distribution and magnitude at the weld centerline. However, increased material removal leads to noticeable changes in through-thickness transverse stress within the weld zone, contrasting with marginal alterations in through-thickness longitudinal stress. Regions distanced from the weld seam show substantial increases in through-thickness longitudinal stress compared to marginal changes in through-thickness transverse stress.

Keywords: residual stress; simulation; welding and machining

check for updates

Citation: Cetintav, I.; Can, Y.; Akkus, N. Investigation of Residual Stress Variation in Sequential Butt Welding and Pocket Material Removal Machining Processes Utilizing Pre-Stress Method: A 3D Simulation Approach. *Metals* **2024**, *14*, 1454. https://doi.org/10.3390/met14121454

Academic Editor: Marek Weglowski

Received: 30 October 2024
Revised: 6 December 2024
Accepted: 10 December 2024
Published: 18 December 2024

1. Introduction

Residual stresses manifest as internal forces inducing material distortions, thereby altering the geometric configuration and mechanical attributes of a material throughout various manufacturing procedures such as heat treatment, machining, or rudimentary forming operations [1–3]. They are delineated as stresses persisting within a component devoid of external loads or thermal differentials [4–6]. Put differently, residual stresses in a structural element denote inherent stress states in the absence of deliberate interventions or external loading conditions [7,8]. These residual stresses are categorized into three distinct types across varying magnitudes, as depicted in Figure 1 below.

Micro-stress distributions delineate the internal stress states within individual grains of a material, whereas meso-stresses characterize the stress distribution at the interfaces between adjacent grains. Macro-stresses, on the other hand, signify the cumulative stress evolution across a multitude of grains. For instance, in welded joints, stress manifestations are commonly observed at the macroscopic level [10,11]. Figure 2 gives an overview of thermomechanical material properties depending on the temperature and microstructural phase. A recent literature review on the subject was performed by Pereira [12], and the figure is repeated here as it is an excellent graphical representation of the problem. Starting from the three main model components needed to simulate heat treatment degradation (heat transfer analysis, phase transformations, and mechanical response), Figure 2 shows their important factors, the issues that need to be addressed and the stages of the most critical results obtained from simulations under weld-like thermal influence and the key influencing factors. Figure 2 is also used as a visual aid to represent the complexity of the processes and clearly shows that each fundamental reason for a finite element solution must be addressed separately.

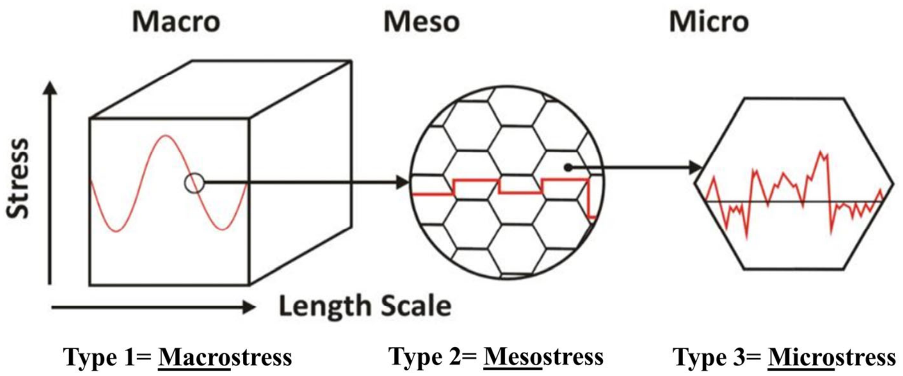

Figure 1. Three different types of residual stresses at different scales. Adapted from Ref. [9].

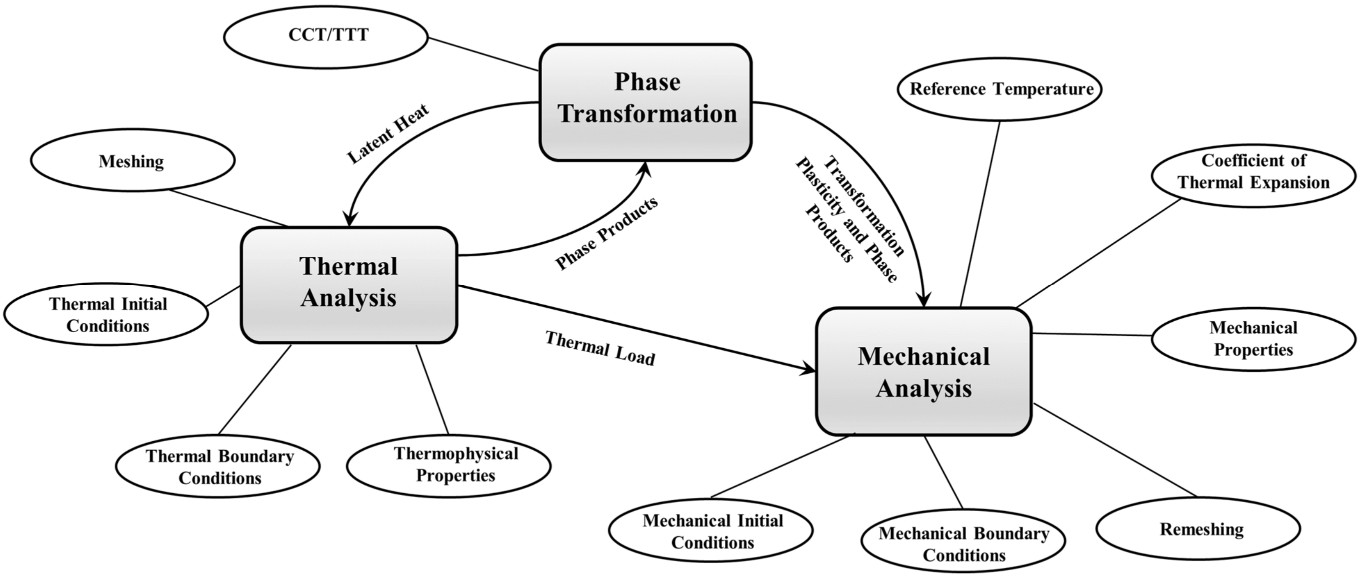

Figure 2. Schematic representation of the main and side effect factors representing the residual stress generation processes.

Manufacturing processes serve as predominant sources of residual stress, wherein nearly all manufacturing procedures—encompassing casting, welding, machining, molding, heat treatment, bending, rolling, or plastic deformation during forging—instigate residual stresses within the fabricated component [13,14]. Additionally, localized material impact resulting from sharp notches or specific surface treatments like sandblasting or surface hardening can induce residual stresses [15]. Various factors contribute to the generation of residual stresses, including the emergence of deformation gradients in disparate regions of the component due to thermal gradients, volumetric alterations during solidification, or solid-state transformations, as well as variations in the coefficient of thermal expansion [16,17]. These residual stresses exert a significant influence on material strength, particularly in the context of fatigue. Thus, it is imperative to extract pertinent information regarding the internal stress state either through direct measurements or via simulation predictions [18,19].

Accurately predicting residual stress and deformation resulting from welding processes holds paramount importance in the manufacturing of mechanical elements [20–22].

Such predictions enhance the reliability of the ensuing component, mitigate errors, and minimize manufacturing costs [23]. Finite element analysis of welding-induced residual stress and deformation constitutes a pivotal phase in the fabrication of mechanical structures and parts, facilitating cost reduction, defect minimization, and component optimization [24–26].

Previous studies by Jang [27], Tran [28], and Hekmatjou [29] utilized thermal–mechanical simulation to predict residual stress in welding processes. While the finite element approach provided valuable insights into temperature effects, the analysis lacked experimental validation, limiting the accuracy of the predictions.

Jin [30] and Gu [31] applied a simplified 2D model for residual stress analysis. The main strength of their approach is computational efficiency; however, its inability to account for complex geometries renders the predictions insufficient for practical industrial applications where 3D characteristics are crucial.

Sarmast [32] and Manai [10] integrated experimental data with simulations to enhance their analysis. While the results were promising, the relatively small sample size could limit the reliability and generalizability of the conclusions derived from their study.

Although several studies have analyzed residual stress using finite element methods, few have integrated a sequential analysis of welding and subsequent machining [33–36], which is essential for understanding the cumulative effects of manufacturing processes.

A review of recent works [37,38] reveals that the majority of research has focused on simulating thermal effects during welding, with limited attention to mechanical interactions during subsequent machining. This creates a significant gap in understanding the evolution of residual stresses in real-world manufacturing scenarios, especially where machining immediately follows welding.

Likewise, in machining processes, residual stress arises from various sources previously delineated. Plastic deformation occurs during chip formation and tool-to-workpiece contact, while thermal gradients stem from frictional heat and plastic deformation [39,40]. Elevated temperatures and pressures can induce phase transformations on the machined surface, further compounded by the interplay of stress and temperature on material behavior during loading [41]. Consequently, the undesirable consequences of residual stress generation on machined surfaces pose challenges in the manufacturing realm, necessitating robust predictive methodologies to enable researchers to surmount them.

The primary aim of this research is to investigate the residual stress evolution in components subjected to sequential butt welding and subsequent material removal machining processes. This study utilizes a 3D simulation approach combined with experimental analysis to provide a deeper understanding of how residual stresses develop and change across these processes. By developing a detailed model of both welding and machining, this research seeks to optimize manufacturing parameters and contribute to improved reliability of mechanical components used in industrial applications, particularly in sectors where stress management is critical, such as aerospace and defense.

The current investigation is intended to serve as a comprehensive resource for the analysis of welded materials harboring residual stresses, particularly in domains such as material behavior, strength assessment, and the manufacturing process, especially in the context of successive production stages involving material removal. This study embodies an interdisciplinary character, spanning material science, strength calculations, and manufacturing processes. The objectives of this research endeavor are delineated as follows:

- To elucidate alterations in stress patterns within materials subjected to elevated temperatures during welding processes, aiming to preempt defects arising post-assembly in operational environments.
- To discern and advocate for efficient and cost-effective manufacturing protocols within the industrial sector.
- To identify application niches within aerospace and defense industries, aiming to optimize manufacturing parameters and ascertain the most efficacious assembly components.
- Through the implementation of optimized parameters, to augment the performance of cutting tools utilized in the manufacturing sphere. This entails conducting com-

parative analyses with prior studies to showcase the advantages conferred by the proposed model and to evaluate its favorable impacts on the operational efficacy of manufacturing machinery.

- The modeling outcomes derived from this study will be instrumental in enhancing the reliability of strength analysis performances. Through comparative assessments with designs from prior studies, the impacts will be scrutinized, aiming to achieve heightened product reliability while minimizing material usage.
- Furthermore, to substantiate the applicability of the obtained results in engineering calculations, a prototype product fabricated under suitable operational conditions will be showcased. This demonstration will serve to underscore the potential benefits attainable in the realms of design and production, thereby elucidating opportunities for leveraging the accrued gains.

2. Materials and Methods

2.1. Experimental Analysis

2.1.1. Welding

In the commencement of the welding process, it is imperative that the materials comprising the constituent parts exhibit a smooth surface, facilitating the generation of a spark from the arc and the establishment of an electrical circuit. Plates and cylindrical components with suitable dimensions were chosen to prevent any roughness on the material surface. These components underwent minimal cutting, and, subsequent to achieving the desired geometries, their surfaces underwent a polishing process.

Preceding the welding procedure, all specimens underwent preheating to specific stress-relieving temperatures and were held at these temperatures for a specified duration to mitigate the risks of distortion and cracking. It is essential to bear in mind that prior stresses and decarburization present in the part can significantly influence the resulting stress state on the surface.

The chemical compositions of the 304 stainless steel base metal and the 308 L filler material are critical in determining their mechanical properties and performance in welding applications (Table 1). The base metal, 304, contains 0.08% carbon, 2% manganese, 1% silicon, 18% chromium, and 10% nickel, with trace amounts of phosphorus (0.045%) and sulfur (0.03%). These elements provide good corrosion resistance, strength, and formability. In contrast, the 308 L filler material has a lower carbon content (0.03%) to reduce the risk of carbide precipitation, enhancing resistance to intergranular corrosion. It contains slightly higher levels of chromium (19.5–22%) and similar nickel content (9–11%), with a small addition of molybdenum (0.75%) and copper (0.75%), improving overall strength and toughness. These variations in composition between the filler and base metal are essential for ensuring optimal weld quality, especially in high-performance applications requiring durability and corrosion resistance.

Table 1. Chemical composition of weld and base metals. Adapted from Ref. [42]

Material	C	Mn	Si	Cr	Ni	P	S	Mo	Cu
304	0.08	2	1	18	10	0.045	0.03	-	-
308 L (Filler)	0.03	1–2.5	0.3–0.65	19.5–22	9–11	0.03	0.03	0.75	0.75

The welding parameters selected for the experiment are outlined in Table 2. Prior to the execution of the actual experiment, a series of trial runs were conducted to ascertain a suitable range of parameters within which welding was feasible, and no observable defects such as undercut and porosity occurred.

Table 2. Welding parameters.

Parameter	Value
Current	180–230 A
Voltage	50 V
Travel Rate	2–3 mm/s
Gas Flow Rate	8–10 (1/min)
Current Type	AC

In the experimental trials, TIG welding with Alternating Current (AC) was employed due to its concentration of heat in the weld area. Zirconiumized tungsten electrodes with a diameter of 3.4 mm were utilized as electrodes for this experiment. The electrode tip underwent grinding to reduce its diameter to 2/3 of the original, followed by the creation of spring tension on a piece of scrap material, resulting in the formation of a ball at the tip of the electrode.

After the specimens were prepared, the plates and tubes were affixed side by side on the worktable using a flexible clamp and were subsequently welded to form a butt joint.

2.1.2. Machining/Material Removal

In the aftermath of the initial assessment of residual stress, the components subjected to welding underwent requisite preparations for subsequent machining. Within the scope of the current dissertation, the machining operation adopted was milling, chosen for its expediency and appropriateness in handling the components. Despite the availability of sophisticated milling machinery, a preference was given to a mechanical milling machine of a type adept at the removal of coarser chips. This selection aimed at enhancing the clarity of residual stress observation. The milling process employed two High-Speed Steel with Cobalt (HSS-E) DIN 844 (Walter AG, Tübingen, Germany) cylindrical handle finger miller–short BN-type milling cutters featuring diameters of 5 and 10 mm. Detailed information on the utilized milling cutters and their respective specifications is delineated in Figure 3.

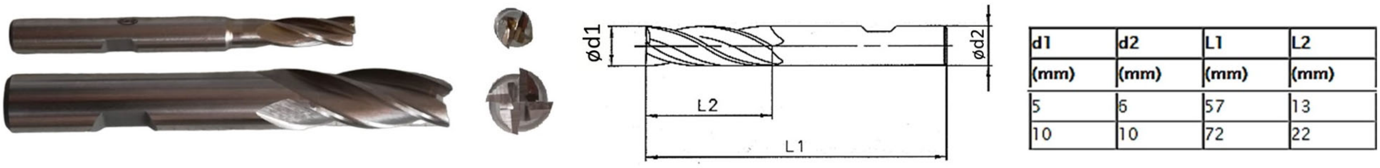

d1 (mm)	d2 (mm)	L1 (mm)	L2 (mm)
5	6	57	13
10	10	72	22

(**a**) (**b**) (**c**)

Figure 3. Representation of milling cutters used—(**a**) Cutter, (**b**) Drawing of Cutter, (**c**) Cutter-related features.

In configuring the milling process parameters, the spindle rotational speed was established at 8000 revolutions per minute (rpm), and the feed rate was set at 0.05 mm per tooth. Considering the varying part thicknesses, specifically 10 mm for quadrilateral components and 3 mm for cylindrical elements, the depths of cut were determined to be 0.5 mm. The outcomes of the milling process are depicted in Figure 4, showcasing the resultant condition of the materials. For the evacuation of large-sized pockets, a preliminary step involved hole-drilling. Furthermore, an examination into the influence of different geometries on residual stress behavior was conducted. Following these procedural steps, all components underwent a secondary assessment of residual stress.

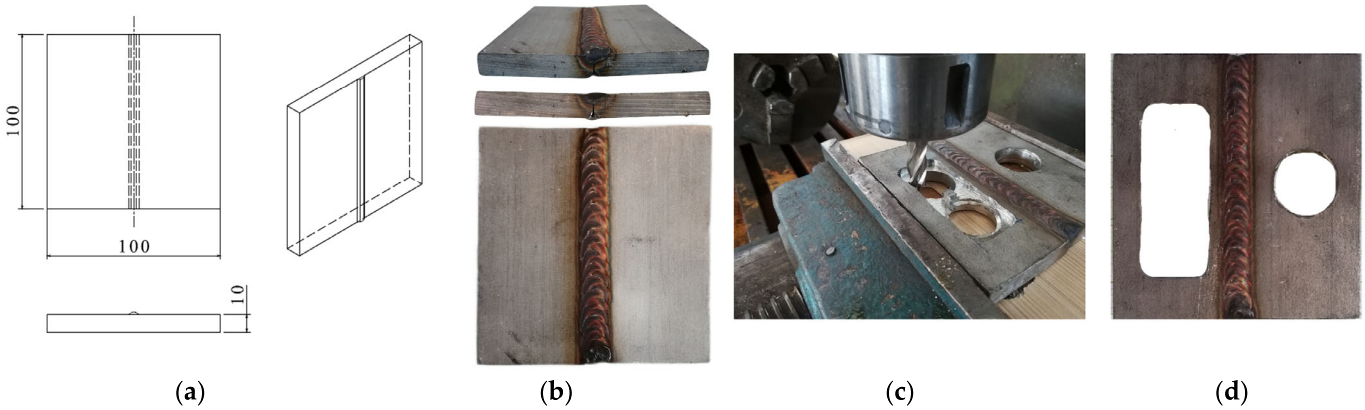

Figure 4. Technical illustration of component, (**a**) Drawing of welded part, (**b**) After welding, (**c**) During machining, (**d**) After machining.

2.1.3. Residual Stress Measurement

Within the context of the current investigation, both the X-ray method and hole drilling techniques were employed as experimental approaches to ascertain the residual stresses subsequent to welding and machining procedures. Given the typical requirement of smooth, lustrous, and level surfaces for effective X-ray analysis, the hole-drilling method was specifically adopted to address irregular areas resulting from welding and machining processes on the components. Incremental Hole Drilling (IHD) was performed using a high-precision Vishay RS-200 device (Vishay Precision Group (VPG), Malvern, AL, USA). The strain gauge data were analyzed using Matlab based on ASTM E837-13a standards [43]. Stress values were averaged over depths ranging from 0.5 mm to 2.0 mm, with incremental steps of 0.5 mm. This depth range was chosen to capture the stress distribution both near the surface and through the thickness, balancing measurement accuracy and resolution. The residual stress profile as a function of depth demonstrated a gradual reduction in magnitude with increasing depth, attributed to the diminishing effects of thermal and mechanical gradients away from the weld and machined surfaces. This observation aligns with the principle that surface and near-surface layers are more significantly affected by welding-induced thermal stresses compared to deeper layers, which exhibit comparatively lower stress magnitudes.

X-Ray Diffraction (XRD) measurements were conducted using a Rigaku SmartLab diffractometer(Rigaku Corporation, Tokyo, Japan) with Cu-Kα radiation at a 1.54 Å wavelength. Stress profiles were calculated using the $\sin^2\psi$ method, and data processing was performed using Rietveld analysis via SmartLab Studio II software(Rigaku Corporation, Tokyo, Japan), commencing with AISI304 material and focusing on crystallographic planes. Residual stress measurements at varying depths were calculated using strain gauge data; X-Ray Diffraction (XRD) was performed, providing near-surface stress measurements. A comparison was made between the through-thickness averages of IHD and near-surface XRD results to validate the accuracy of the simulation.

2.2. Mathematical Model

The determination of residual stresses arising from welding and material removal processes typically involves the utilization of finite element methodologies. Theoretical frameworks for evaluation may encompass both thermal and mechanical models, allowing for comprehensive analysis and understanding of the underlying phenomena. Figure 5 illustrates the analytical procedures outlined below.

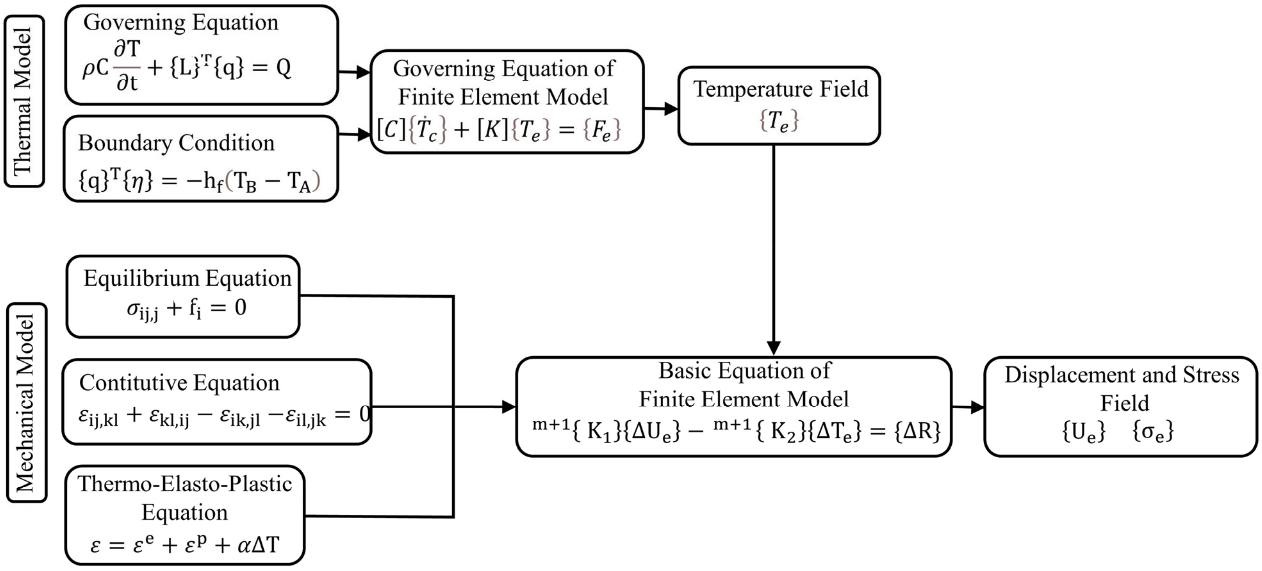

Figure 5. Thermomechanical analysis procedures for welding and material removal.

A control volume is delineated by an arbitrary surface; the basic equation of heat conduction is as follows:

$$\rho C\frac{\partial T}{\partial t}=\{L\}^{\mathrm{T}}([D]\{L\}T)+Q=\frac{\partial}{\partial x}\left(k_x\frac{\partial T}{\partial x}\right)+\frac{\partial}{\partial y}\left(k_y\frac{\partial T}{\partial y}\right)+\frac{\partial}{\partial z}\left(k_z\frac{\partial T}{\partial z}\right)+Q \tag{1}$$

And the heat convection over the surface of the control volume, which is the main boundary condition, is as follows:

$$\{q\}^T\{\eta\}=-h_{\mathrm{f}}(T_{\mathrm{B}}-T_{\mathrm{A}}) \tag{2}$$

where variables such as ρ represent density, C denotes specific heat, T signifies temperature, t denotes time, {q} denotes heat flux, Q represents the internal heat generation rate, η denotes the unit outward normal vector, h_f indicates the film coefficient, T_B represents the bulk temperature of the adjacent fluid, and T_A denotes the temperature at the surface of the model.

Considering the governing equation as a differential temperature change dT, integrating over the volume of this differential element and adding the boundary condition makes Equation (1) as follows:

$$\int_V\left(\delta T\rho C\frac{\partial T}{\partial t}\right)\mathrm{d}V+\int_V\left(\delta T\{L\}^{\mathrm{T}}[D]\{L\}T\right)\mathrm{d}V=\int_V(\delta TQ)\mathrm{d}V+\int_A(\delta Th_{\mathrm{f}}(T_{\mathrm{B}}-T_{\mathrm{A}}))\mathrm{d}A \tag{3}$$

If temperature (T) is allowed to vary in space and time, Equation (3) will take the following form:

$$\rho\int_V\left(C[N][N]^{\mathrm{T}}\left\{\dot{T}_{\mathrm{e}}\right\}\right)\mathrm{d}V+\int_V\left([B]^{\mathrm{T}}[D][B]\{T_{\mathrm{e}}\}\right)\mathrm{d}V=\int_A[N]Q\mathrm{d}V+\int_V[N]h_{\mathrm{f}}\left(T_{\mathrm{B}}-[N]^T\{T_{\mathrm{e}}\}\right)\mathrm{d}A \tag{4}$$

where $\{T_e\}$ is called the node temperature vector and [N] is called the element shape function. Equation (4) can be abbreviated as follows:

$$[C]\left\{\dot{T}_{\mathrm{e}}\right\}+[K]\{T_{\mathrm{e}}\}=\{F_{\mathrm{e}}\} \tag{5}$$

$$[C]=\rho\int_V C[N]^{\mathrm{T}}[N]\mathrm{d}V \tag{6}$$

$$[K]=\int_V[B]^{\mathrm{T}}[D][B]\mathrm{d}V+\int_A h_{\mathrm{f}}[N][N]^{\mathrm{T}}\mathrm{d}A \tag{7}$$

$$\{F_\mathrm{e}\} = \int_V Q[N]\mathrm{d}V + \int_A h_\mathrm{f} T_\mathrm{B}[N]\mathrm{d}A \tag{8}$$

The temperature field obtained from these equations will be added to the mechanical model.

In accordance with the fundamental principles of virtual work and the divergence theorem, the expressions governing equilibrium and constitutive relationships may be reformulated into a matrix representation.

$$\int_V \{\delta\varepsilon\}^T\{\sigma\}\mathrm{d}V = \int_A \{\delta u\}^T\{P\}\mathrm{d}A + \int_V \{\delta u\}^T\{f\}\mathrm{dV} \tag{9}$$

where

$$\{\varepsilon\} = [B]\{U_\mathrm{e}\}, \{\delta\varepsilon\} = [B]\{\delta U_\mathrm{e}\} \tag{10}$$

$$\{u\} = [N]\{U_\mathrm{e}\} \tag{11}$$

$$[B] = [L][N] \tag{12}$$

The variables involved are as follows: {P} denotes the surface force vector, {f} represents the body force vector, {u} signifies the displacement vector, {ε} stands for the strain vector, {σ} denotes the stress vector, $\{U_\mathrm{e}\}$ represents the nodal displacement vector, [B] denotes the strain–displacement matrix, [N] signifies the matrix of the shape function, and [L] denotes the differential operator matrix.

Combining the equations above:

$$\int_V [B]^\mathrm{T}\{\sigma\}\mathrm{d}V = \{R\} = [K]\{U_\mathrm{e}\} \tag{13}$$

$$\{R\} = \int_A [N]^\mathrm{T}\{P\}\mathrm{d}A + \int_V [N]^\mathrm{T}\{f\}\mathrm{d}V \tag{14}$$

$$\{K\} = \int_V [B]^\mathrm{T}\{D^\mathrm{e}\}[B]\mathrm{d}V \tag{15}$$

{R} refers to the nodal equilibrium external force matrix, while {K} represents the stiffness matrix.

In the context of a linear elastic model, the provided expressions are valid. However, in elastoplastic analysis, where nodal displacement functions exhibit nonlinearity, an incremental approach is adopted. For incremental analysis, the load {R} at step (m + 1) can be formulated as follows:

$$^{m+1}\{R\} = {}^{m}\{R\} + \{\Delta R\} \tag{16}$$

Given that the solutions of $^\mathrm{m}\{U_\mathrm{e}\}$, $^\mathrm{m}\{\sigma_\mathrm{e}\}$, and $^\mathrm{m}\{\varepsilon_\mathrm{e}\}$ at the *m*th step are presumed to be known, the solutions of the (*m* + 1)th step can subsequently be obtained as follows:

$$^{m+1}\{U_\mathrm{e}\} = {}^{m}\{U_\mathrm{e}\} + \{\Delta U_\mathrm{e}\} \tag{17}$$

$$^{m+1}\{\sigma_\mathrm{e}\} = {}^{m}\{\sigma_\mathrm{e}\} + \{\Delta\sigma_\mathrm{e}\} \tag{18}$$

In accordance with this, Equations (13) and (16) transform to

$$\int_V [B]^\mathrm{T}\{\Delta\sigma_\mathrm{e}\}\mathrm{d}V = {}^{m}\{R\} + \{\Delta R\} - \int_V [B]^\mathrm{T} m\{\sigma_\mathrm{e}\}\mathrm{d}V \tag{19}$$

Upon substitution of Equation (13) into Equation (19), the resulting expression is obtained.

$$\int_V [B]^\mathrm{T}\{\Delta\sigma_\mathrm{e}\}\mathrm{d}V = \{\Delta R\} \tag{20}$$

The thermal elastoplastic material model, which adheres to the von Mises yield criterion and the isotropic strain hardening rule, is under consideration. The stress–strain relations can be expressed as follows:

$$\{\Delta\sigma_{\mathrm{e}}\} = \{D^{\mathrm{ep}}\}[B]\{\Delta U_{\mathrm{e}}\} - \left\{C^{\mathrm{th}}\right\}[M]\{\Delta T_{\mathrm{e}}\} \tag{21}$$

$$\{D^{\mathrm{ep}}\} = \{D^{\mathrm{e}}\} + \{D^{\mathrm{p}}\} \tag{22}$$

In the provided context, the following notations apply: {Dje} represents the nodal stress increment matrix, {Dεe} denotes the nodal strain increment matrix, {DT} signifies the temperature increment matrix, {De} stands for the elastic stiffness matrix, {Dp} represents the plastic stiffness matrix, {Cth} denotes the thermal stiffness matrix, {DTε} signifies the nodal temperature increment matrix, and [M] represents the temperature shape function.

Upon substituting Equation (21) into Equation (20), the resultant expression is derived.

$$^{m+1}\{K_1\}\{\Delta U_{\mathrm{e}}\} - {}^{m+1}\{K_2\}\{\Delta T_{\mathrm{e}}\} = \{\Delta R\} \tag{23}$$

$$^{m+1}\{K_1\} = \int_V [B]^{\mathrm{T}}\{D^{\mathrm{ep}}\}[B]\mathrm{d}V \tag{24}$$

$$^{m+1}\{K_2\} = \int_V [B]^{\mathrm{T}}\left\{C^{\mathrm{th}}\right\}[M]\mathrm{d}V \tag{25}$$

The displacement increment {ΔUe} and stress increment {Δje} can be derived from Equations (14) and (15), respectively. Utilizing these outcomes, the displacement {Ue} and stress {je} can subsequently be determined employing Equations (17) and (18).

3. Finite Element Analysis

This study utilized MSC Mentat software (version 2016) as both the pre- and post-processor, and MSC Marc software (version 2016) as the Finite Element Method (FEM) solver. MSC.Marc, a commercially available nonlinear FEM software package, possesses robust capabilities tailored for the simulation of welding and machining processes. Within MSC Marc Mentat software (version 2016), bespoke model definition functionalities cater to the intricacies of welding and machining simulations. These processes, characterized by both thermal and mechanical dynamics, necessitate meticulous specification of boundary conditions. Such conditions encompass parameters such as welding flux definition, weld path determination, filler metal selection, and tool path assignment for machining operations. Noteworthy among the predefined thermal sources is the Goldak double ellipsoidal heat source model, utilized for simulating welding processes. Additionally, filler metal deposition is governed by mechanisms of element activation and deactivation. Toolpaths guiding machining operations are generated using CATIA V6 software, a Computer-Aided Design (CAD) platform, and subsequently imported into MSC Marc Mentat software (version 2016) through FORTRAN subroutines.

Reverse plasticity was modeled using kinematic hardening in the finite element simulation to capture the Bauschinger effect. This approach ensures realistic redistribution of residual stresses during machining, accounting for the material's ability to reverse plastic deformation under unloading.

Supplementary features augmenting analytical capabilities within MSC.Marc encompass time-stepping, convergence control, and adaptive meshing functionalities. Adaptive time-stepping was judiciously employed within the welding and machining models, wherein the determination of rise time was predicated on the permissible temperature alteration per incremental step. Convergence criteria were deliberately relaxed to expedite the modeling process, albeit without compromising result accuracy. The nonlinear material properties, contingent upon temperature, are cataloged in Table 3.

Table 3. Temperature-dependent properties of AISI 304 material. Adapted from Ref. [42]

Temperature °C	Thermal Expansion Coefficient °C^{-1}	Young's Modulus GPa	Specific Heat J/g °C	Yield Strength (MPa)	Thermal Conductivity J/mm °C s	Poisson Ratio
−100	1.33×10^{-5}	206	0.394	270	0.0117	0.294
0	1.58×10^{-5}	198	0.463	265	0.014	0.295
20	1.61×10^{-5}	196	0.472	265	0.0145	0.301
100	1.72×10^{-5}	190	0.501	218	0.016	0.310
200	1.81×10^{-5}	182	0.525	186	0.0176	0.318
300	1.88×10^{-5}	174	0.532	170	0.0191	0.322
400	1.95×10^{-5}	166	0.555	155	0.0204	0.325
500	2.01×10^{-5}	158	0.582	149	0.0219	0.326
600	2.07×10^{-5}	150	0.604	105	0.0233	0.329
700	2.13×10^{-5}	142	0.610	95	0.0247	0.331
800	2.19×10^{-5}	134	0.610	91	0.0261	0.334
1500	2.19×10^{-5}	78	0.610	10	0.0261	0.337
1600	2.19×10^{-5}	10	0.610	10	0.0261	0.388

Similar to customary finite element analyses, the initial phase entails the creation of geometric representations and the establishment of an element mesh. This task was undertaken utilizing MSC.Mentat, owing to its intuitive interface and robust suite of geometry and mesh generation tools. Notably, MSC.Mentat serves as the primary pre- and post-processor for MSC.Marc.

The finite element model shown in Figure 6 was built using the four-node solid element type 7 from MSC.Marc, which provides a robust framework for capturing the mechanical and thermal behaviors during the welding and machining processes. The number of degrees of freedom per element includes both translational and rotational degrees, with each node having six degrees of freedom (three translational and three rotational) to adequately capture deformations and stress evolution throughout the simulation.

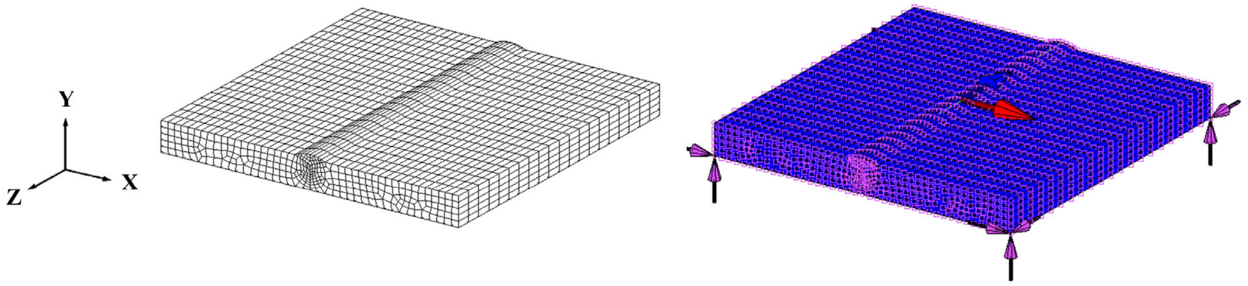

(**a**) (**b**)

Figure 6. Representation of the (**a**) node and elements of the meshed part and (**b**) welding (red arrow) and clamp boundary condition (pink arrow).

The model consisted of a total of 12,755 elements and 7035 nodes. The mesh was refined in regions of high thermal and mechanical activity—such as near the weld seam and the areas influenced by machining—to capture detailed stress and strain variations. Finer mesh elements were used in these critical areas to ensure high accuracy, while coarser elements were used in regions with less activity to optimize computational efficiency.

Furthermore, an adaptive meshing technique was implemented during the machining phase to handle the material removal dynamically. This adaptive meshing allowed for local refinement in areas undergoing significant deformation due to the cutting tool, enhancing the accuracy of the stress and deformation predictions. The adaptive meshing strategy ensured that the element size automatically adjusted based on the evolving conditions during the machining process, particularly in the areas impacted by the milling operation.

The mesh size for the model was determined based on sensitivity analysis, with finer elements (1 mm) used in critical zones such as the weld seam and machining areas, and coarser elements (5 mm) elsewhere. For machining, the removal depth was 2 mm, modeled with five elements per layer, ensuring a balance between computational efficiency and accuracy. The material removal process was simulated incrementally, with equilibrium checks performed after each element layer removal to maintain accuracy.

The mesh quality was evaluated using standard criteria, such as element aspect ratio (<2), skewness (<0.5), and Jacobian determinant (>0.6). Quadratic temperature distributions were implemented using four-node solid elements with three integration points across the thickness. Mesh refinement was applied in the weld seam and machining areas, with element sizes ranging from 1 mm to 5 mm. Critical zones used circular perimeter meshes with at least five elements per 2 mm depth to ensure accurate stress redistribution during machining.

Quadratic temperature distributions through the thickness of the elements were implemented utilizing four-node solid elements in the analysis. These elements offer the flexibility of selecting from three integration points across the element thickness, thus affording a precise estimation of temperature distribution within the slab. Demonstrating suitability for both thermal and coupled thermal–structural analyses, these elements serve as a robust choice. Within the framework of MSC.Marc, a numerical analysis protocol has been devised to anticipate distortion arising from 3D batch-machining operations. This analytical framework enables engineers to refine structural designs and optimize machining processes. Central to this procedure is the presumption that the perturbations induced by the cutting process remain localized and insignificantly impact pre-existing residual stresses.

As shown in Figure 6, the model was fixed by applying boundary conditions at the bottom edges of the plate. Specifically, nodes along the bottom edge were constrained in all three translational directions to prevent movement, simulating a clamped condition. Additionally, displacement constraints were applied along the sides of the plate to prevent rigid body motion while allowing thermal expansion to occur freely in the vertical direction. This fixing approach accurately represents the physical clamping used in experimental conditions to mimic real-life scenarios.

Welding, as a thermal process, is governed by specific boundary conditions meticulously defined through various model options such as WELD PATH, WELD FILL, and WELD FLUX. These options enable the determination of the weld heat input-employing technique; heat input can be modeled as a spatially varying temperature boundary condition, implemented through the WELD FILL model definition option, and applied specifically to the nodes of the filling elements. In this scenario, the flux value, typically set to zero power, is omitted from the WELD FLUX model identification option. Notably, this methodology finds frequent application within the context of this work.

The WELD FLUX, which represents the heat flux option, utilized Goldak's double ellipsoidal geometry (Figure 7) heat source [44], as discussed previously, to delineate volume fluxes in both 2D and 3D configurations.

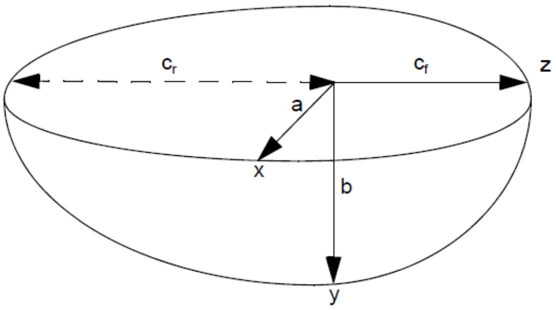

Figure 7. Goldak's Double Ellipsoidal Source Flux showing Local Coordinate Dimensions.

$$q_f(x,y,z) = Q_0 \cdot \frac{6\sqrt{3}.f_\xi}{a.b.c_f.\pi^{\frac{3}{2}}} \exp\left(-\frac{3x^2}{a^2}\right).\exp\left(-\frac{3y^2}{b^2}\right).\exp\left(-\frac{3z^2}{c^2}\right) \quad (26)$$

$$q_r(x,y,z) = Q_0 \cdot \frac{6\sqrt{3}.f_\xi}{a.b.c_r.\pi^{\frac{3}{2}}} \exp\left(-\frac{3x^2}{a^2}\right).\exp\left(-\frac{3y^2}{b^2}\right).\exp\left(-\frac{3z^2}{c^2}\right) \quad (27)$$

$$f_\mathrm{f} + f_\mathrm{r} = 2 \quad (28)$$

$$f_\mathrm{f} = \frac{2}{1 + \frac{c_\mathrm{r}}{c_\mathrm{f}}} \quad (29)$$

$$f_\mathrm{r} = \frac{2}{1 + c_\mathrm{f}/c_\mathrm{r}} \quad (30)$$

Upon completion of the welding process, several methodologies exist for introducing initial stresses into the Finite Element (FE) model, constituting a crucial step in this study for propagating residual stresses into subsequent processes, notably machining. Typically, MSC.Marc offers users the flexibility to incorporate initial stresses through the INIT STRESS model definition option. Additionally, it provides the ability to import data via the PRE STATE option, allowing users to transfer information such as strain and stress from prior analyses to subsequent models. Through the INIT STRESS option, users can specify stresses based on input values or tables, accommodating scenarios where stresses are defined as a function of coordinates. Furthermore, MSC.Marc facilitates the definition of initial stresses via an ASCII-formatted text file, wherein raw initial stress data of randomly situated points within a spatial field are provided. Subsequently, MSC.Marc processes and interpolates the given initial stress data onto the finite element mesh, aligning with the respective location of each element.

The machining process was modeled using CATIA to generate tool paths for pocket evacuation. The removal of square patterns on the top surface was achieved through adaptive meshing, where elements along the circular perimeter were refined to maintain geometric fidelity. The first removal layer was from 10 mm to 8 mm depth, corresponding to five layers per 2 mm depth. Equilibrium was checked after the removal of each element layer to ensure the accuracy of stress redistribution simulations. This incremental approach minimizes errors associated with abrupt changes in boundary conditions. The simulation process leverages cutter geometry and path details extracted from Numerical Control (NC) part-machining data. Utilizing the cutter travel information, an estimation of the material to be removed is made by automatically eliminating the finite elements encompassed within the cutter's path. Subsequently, recalculating the equilibrium allows for the estimation of the distortion in the remaining component. Within the framework of Marc, an interface has been devised to convert cutter path data into finite elements earmarked for removal. Those cutter path data are typically stored in either the Automatically Programmed Tools (APT) source format or the Cutter Location (CL) data format. The APT source format comprises NC data output by Computer-Aided Design (CAD) software such as CATIA (Figure 8). Conversely, CL data represent the cutter's positional information provided by APT compilers.

The dimensions of the cutter shape and its trajectory significantly influence the volume of material to be machined. The cutter's geometry is characterized by the CUTTER expression delineated within the Automatically Programmed Tools (APT) source or Cutter Location (CL) files. The comprehensive representation of the CUTTER expression is articulated as follows (Figure 9):

CUTTER/d, r, e, f, α, β, h

where d represents the tool diameter, r denotes the radius of the corner circle, which can assume values equal to or greater than zero, e signifies the radial distance from the tool axis to the center of the corner circle, f indicates the distance from the tool's endpoint to the center of the corner circle, measured parallel to the tool axis, α denotes the angle from a radial line through the tool's endpoint to the lower line segment, confined within the range of zero to 90°, and assumes positive values, β signifies the angle between the upper segment and the tool axis, within the range of −90° to 90°, and h represents the cutter's height measured from the tool's endpoint along the tool axis.

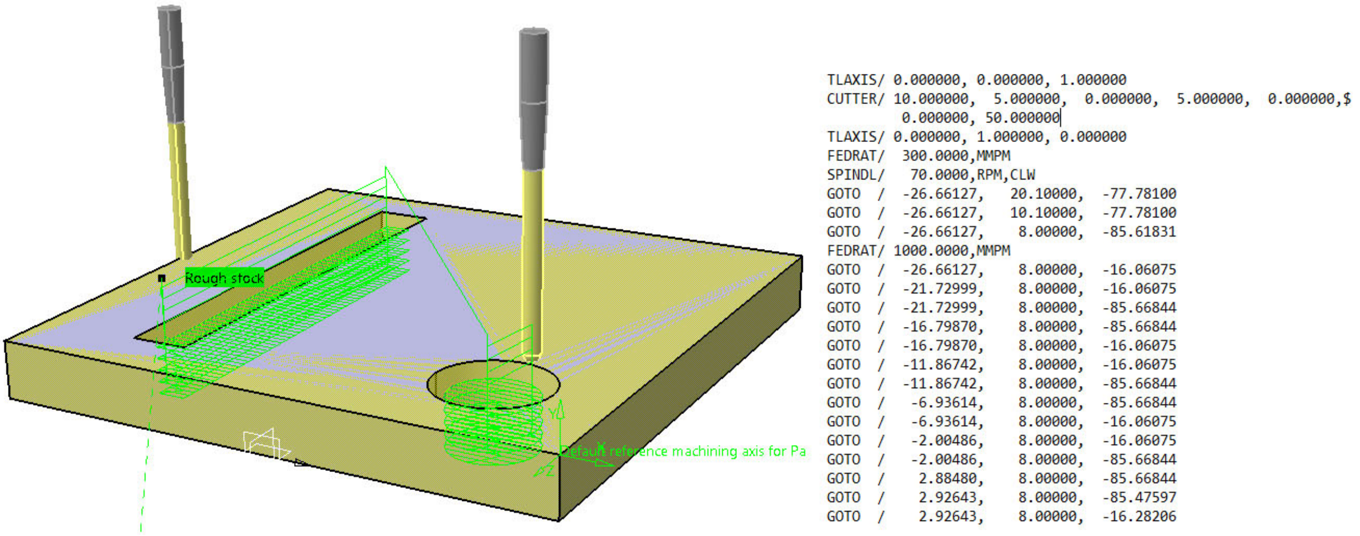

```
TLAXIS/ 0.000000, 0.000000, 1.000000
CUTTER/ 10.000000,  5.000000,  0.000000,  5.000000,  0.000000,$
         0.000000, 50.000000
TLAXIS/ 0.000000, 1.000000, 0.000000
FEDRAT/  300.0000,MMPM
SPINDL/   70.0000,RPM,CLW
GOTO  /  -26.66127,   20.10000,  -77.78100
GOTO  /  -26.66127,   10.10000,  -77.78100
GOTO  /  -26.66127,    8.00000,  -85.61831
FEDRAT/ 1000.0000,MMPM
GOTO  /  -26.66127,    8.00000,  -16.06075
GOTO  /  -21.72999,    8.00000,  -16.06075
GOTO  /  -21.72999,    8.00000,  -85.66844
GOTO  /  -16.79870,    8.00000,  -85.66844
GOTO  /  -16.79870,    8.00000,  -16.06075
GOTO  /  -11.86742,    8.00000,  -16.06075
GOTO  /  -11.86742,    8.00000,  -85.66844
GOTO  /   -6.93614,    8.00000,  -85.66844
GOTO  /   -6.93614,    8.00000,  -16.06075
GOTO  /   -2.00486,    8.00000,  -16.06075
GOTO  /   -2.00486,    8.00000,  -85.66844
GOTO  /    2.88480,    8.00000,  -85.66844
GOTO  /    2.92643,    8.00000,  -85.47597
GOTO  /    2.92643,    8.00000,  -16.28206
```

Figure 8. Definition of tool paths and tool geometry through CATIA.

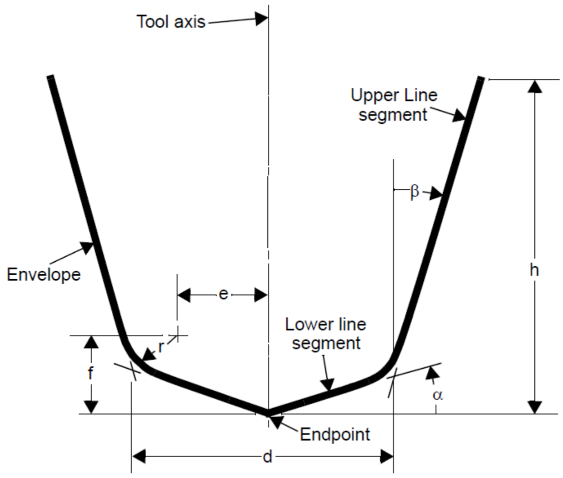

Figure 9. Definition of cutting tool geometry in MSC.Marc software.

The tool cutting path used for both the experimental and simulation procedures was identical. Tool paths were generated in CATIA and subsequently imported into MSC.Marc for use in the finite element simulations, ensuring consistency between the physical and simulated setups.

Figure 10 presents the flowchart delineating the simulation methodology implemented in the present thesis, detailing the establishment of initial and boundary conditions alongside pivotal subroutines. The foremost consideration emphasized in this schematic is the meticulous utilization of the pre-stress routine, which serves as a cornerstone in seamlessly integrating stress states originating from the welding phase into the subsequent machining process. This routine enables the precise transference of stress states derived during welding to the machining phase, ensuring a comprehensive representation of the structural response. Another critical aspect pertains to the precise determination of tool geometry and paths within the CATIA program to faithfully replicate experimental conditions. CATIA provides the modeled tool geometry and paths encoded in a specific format, typically received as ASCII in APT or CCL source code. These codes undergo necessary adjustments and alignment to adhere to the NC Machining subroutine. Further details regarding boundary and initial conditions are meticulously tailored based on experimental insights and aligned with the inherent dynamics of the welding and machining processes.

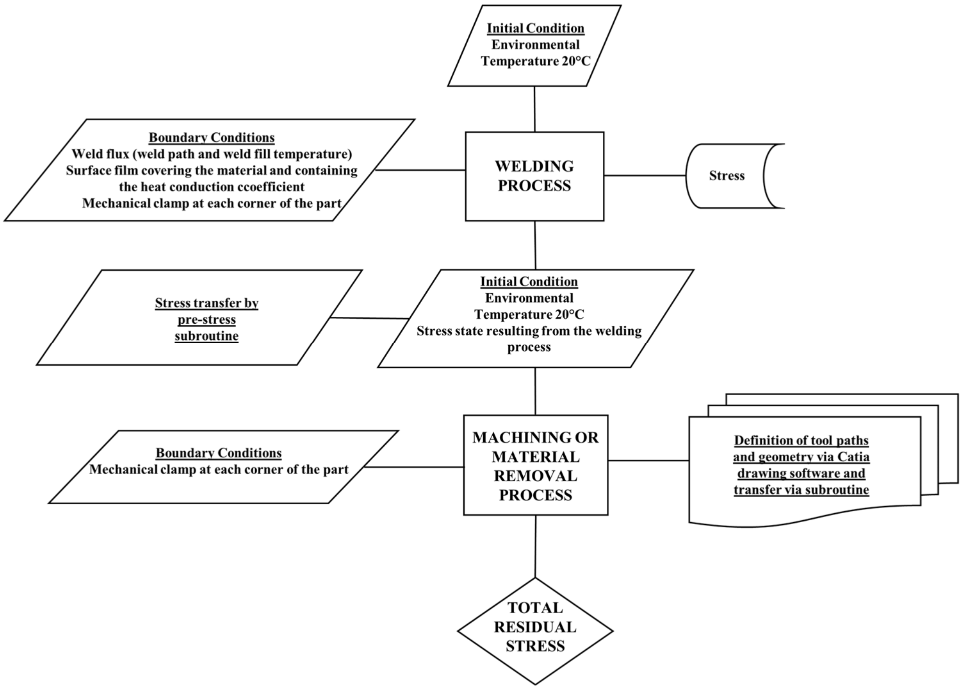

Figure 10. Flowchart of the whole procedure.

4. Results and Discussion

In the present study, a flexible framework was developed on which welding and machining processes could be simulated and residual stress transferred between the two processes. As an application problem, welding and machining processes were simulated to verify the accuracy and physical consistency of the framework. The mathematical framework was validated with the data obtained from the experimental studies. Since the main objective of the study was to transfer residual stresses between two different processes, some conditions affecting the results were ignored. For example, since high temperature gradients occur in both processes, phase transformations occur, and although these transformations increase the sensitivity of the residual stresses, they are generally related to the microstructure. For this reason, phase transformations were neglected in the present study.

IHD and XRD were used as complementary techniques to measure residual stress. While IHD provides stress profiles through the material thickness, XRD measures near-surface stresses with high resolution. To compare these methods, the through-thickness stress distributions from IHD were averaged and correlated with the XRD results. The comparison of IHD and XRD data revealed consistent trends in residual stress redistribution, with minor discrepancies attributed to the different depth sensitivities of the methods. The simulation results closely matched the experimental values, validating the adequacy of the mesh and the step-removal strategy.

Welding and machining residual stresses have a positive or negative effect on the strength of the component, depending on their type, sign, direction, and distribution. Triaxial tensile residual stresses in combination with crack-like defects promote brittle fracture. Uniaxial or biaxial tensile residual stresses reduce corrosion resistance and increase the stability limit, while compressive residual stresses increase fatigue strength. Components with residual welding stresses can fail during subsequent machining, storage, and service loading. A particularly disturbing effect is back spring or spring deformation during machining. Weld distortion reduces the fatigue strength and limit load of components. Due to distortion after welding and machining, specified manufacturing tolerances can be exceeded. Therefore, it is necessary to minimize welding and machining residual stresses and distortions or control them as far as possible according to the relevant requirements.

Figure 11 shows the longitudinal stresses of the part in the z-axis direction after welding and after machining. Longitudinal stresses, as mentioned in the previous sections, are the stresses that cause changes in the length direction of the deforming forces acting on the parts. These stresses are quite high since the welding direction is the same axis. As can be seen, they are positive on the weld seam and in the HAZ region and negative in the remaining parts.

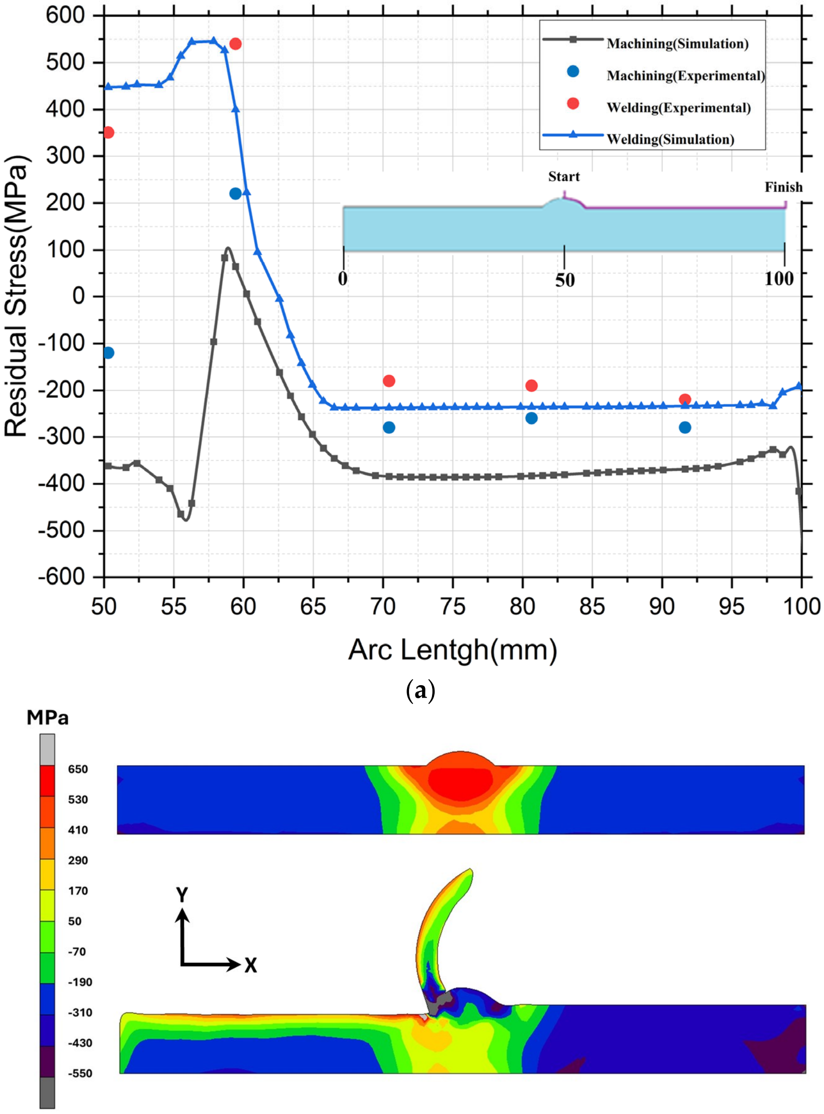

(**a**)

(**b**)

Figure 11. Residual stress distribution in welded and machined components in a 2D simulation: Longitudinal stresses (**a**) Graphical representation of residual stress in the z-direction (longitudinal), (**b**) Distribution of σ_{zz} post-welding and machining process.

Stress distribution along the longitudinal direction (σ_{zz}) with distance (mm) on the x-axis and stress (MPa) on the y-axis is shown. Data points represent through-thickness IHD averages compared with XRD surface measurements and simulation results.

The residual stress measurements presented in Figure 11 were performed every 10 mm away from the weld centerline using the X-ray diffraction (XRD) technique. The experimental results are compared to the simulation values at corresponding locations.

Figure 11 clearly shows that the experimental results and simulation results coincide in the part. Just in front of the weld seam, 10 mm away from the weld center line, the stress value was measured as 352 MPa. The simulation value was calculated as 455 MPa. The chip removal process was designed as orthogonal, i.e., perpendicular cutting in two dimensions, and removed chips at a depth of 2 mm.

Figure 12 shows the longitudinal stress (z-direction) of the part after simulation of three-dimensional welding and orthogonal cutting. As a result of the milling process, a quadrilateral pocket to the left of the weld and a small circular pocket geometry to the right of the weld appeared. The pockets opened after the milling process in Figure 12 are shown as 0—a straight line—in the residual stress graph. The measured values and simulation values after welding and machining show high accuracy. The residual stress value at the point directly above the weld line after welding was measured as 357 MPa, while the corresponding simulation value was 442 MPa. The graph drawn with the simulation values taken from the center line of the material after the welding process coincides with the standard welding stress graphs. After machining, the residual stress values on the same line decrease in the weld area and increase in the areas away from the weld and in the pocket evacuated areas. This is due to the increase in local positive stresses in the areas cut by the milling cutter. Around the weld seam, the post-machining stresses are higher on the small circular pocket side and lower on the quadrilateral pocket side.

Figures 11 and 12 represent different experimental setups to investigate symmetry and stress distribution. Figure 11 focuses on residual stresses near x = 0, while Figure 12 examines stresses near x = 50. These setups allow for the comparison of stress gradients at varying distances from the weld seam. The observed symmetry in the results validates the simulation model, while minor differences highlight localized machining effects.

The yield strength of AISI 304 stainless steel is approximately 270 MPa. As seen in Figure 12, the residual stress values in the weld and machined regions approach the yield strength, particularly after the machining process. This indicates that the material in these regions may be at risk of yielding under operational loads, especially where the residual stresses are tensile.

Figure 13 shows the transverse stress (x-direction) of the part after simulation of three-dimensional welding and milling and cutting processes. The transverse stress values are considerably lower than the longitudinal stress values. After machining, they have almost completely evolved into negative stress, as shown in Figure 13. The highest transverse stress value for the part was measured as 301 MPa 10 mm to the left of the weld seam after welding. The corresponding simulation value was 232 MPa. At the same point, the experimental stress value decreased to 52 MPa after machining. The simulation value was taken as 34 MPa. The residual stress curve after welding and machining simulation coincides with the known curves. Local stress increases after machining are not very evident in the transverse stress graph.

Figure 6 highlights the distinct directional differences in residual stresses. σ_{xx} exhibits compressive behavior, particularly in the middle of the weld, where it reaches a peak of approximately -300 MPa at the boundary with the plate, as corroborated by Figure 13. In contrast, σ_{zz} displays tensile behavior, reaching 380 MPa at the weld center and increasing to 500 MPa at the boundary with the plate, as shown in Figure 12. These differences are attributed to the anisotropic nature of stress distribution in welded components, where longitudinal stresses are influenced predominantly by heat flow along the weld direction, while transverse stresses arise from lateral constraints imposed during cooling. This directional dependency underscores the complexity of residual stress redistribution in welded structures.

Figures 14 and 15 show the longitudinal and von Mises stress distribution of the part after welding and three different machining processes. As can be seen, the residual stress variations are highly dependent on where the milling cutter cuts the material. In each cut, the part reduces the residual stresses with a stress relief effect, but an uneven stress distribution is observed compared to the residual stress distribution in the welding process. This shows the importance of the location of the machining process.

Figure 14 highlights the reduction of longitudinal residual stresses (σ_{zz}) through machining, achieved by breaking the continuity of the weld line. The results show that machining effectively redistributes stresses, reducing tensile residual stresses in the weld seam and adjacent areas. This stress relief mechanism demonstrates a potential method for enhancing structural integrity in welded components. The findings also suggest that similar stress reduction effects could be achieved through alternative approaches, such as intermittent welding [45], which inherently interrupts the weld line and may serve as a cost-effective solution to mitigate residual stresses.

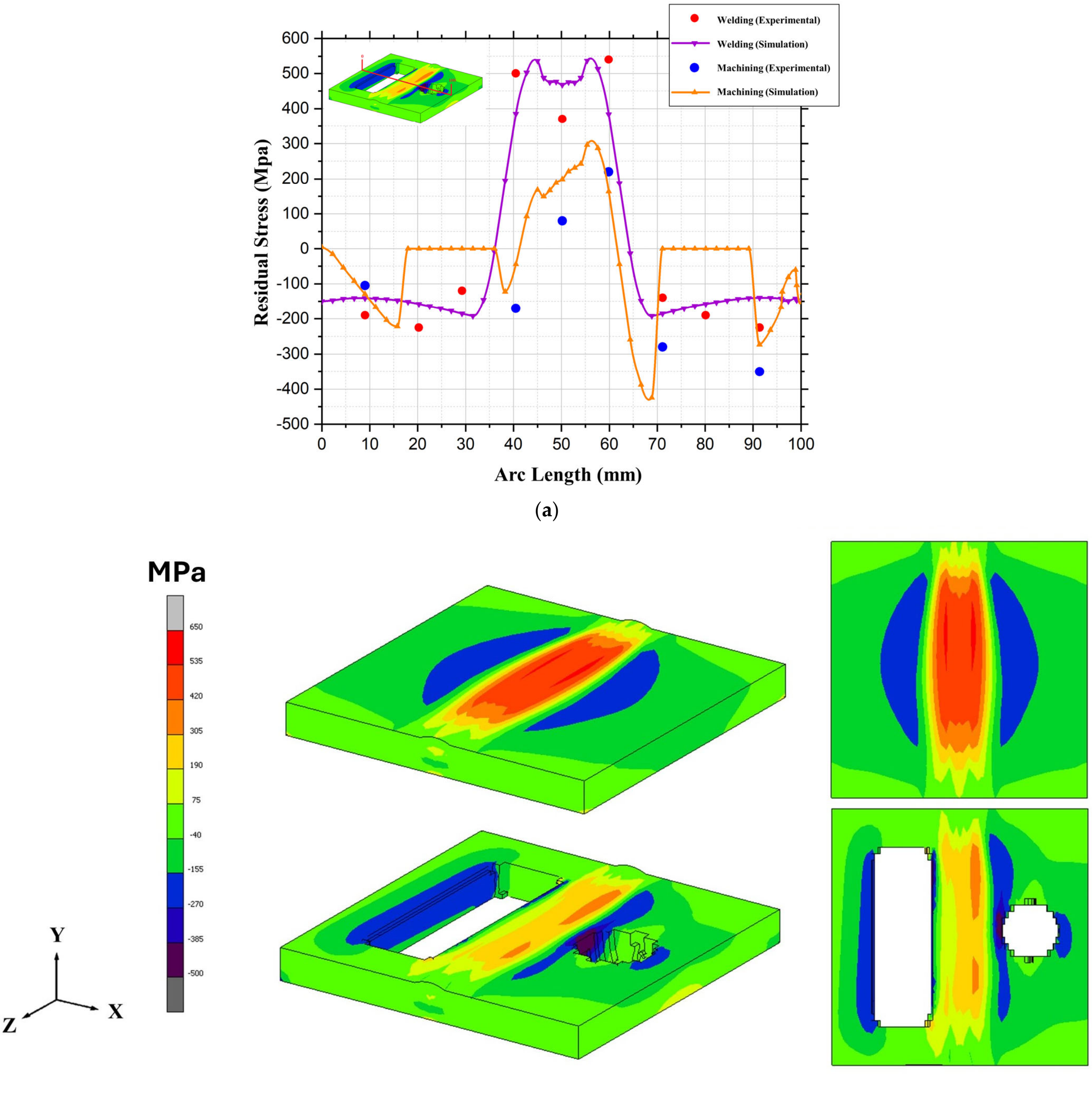

(**a**)

(**b**)

Figure 12. Residual stress distribution in welded and machined components in a 3D simulation: Longitudinal stresses (**a**) Graphical representation of residual stress in the z-direction (longitudinal), (**b**) Distribution of σ_{zz} post-welding and machining process.

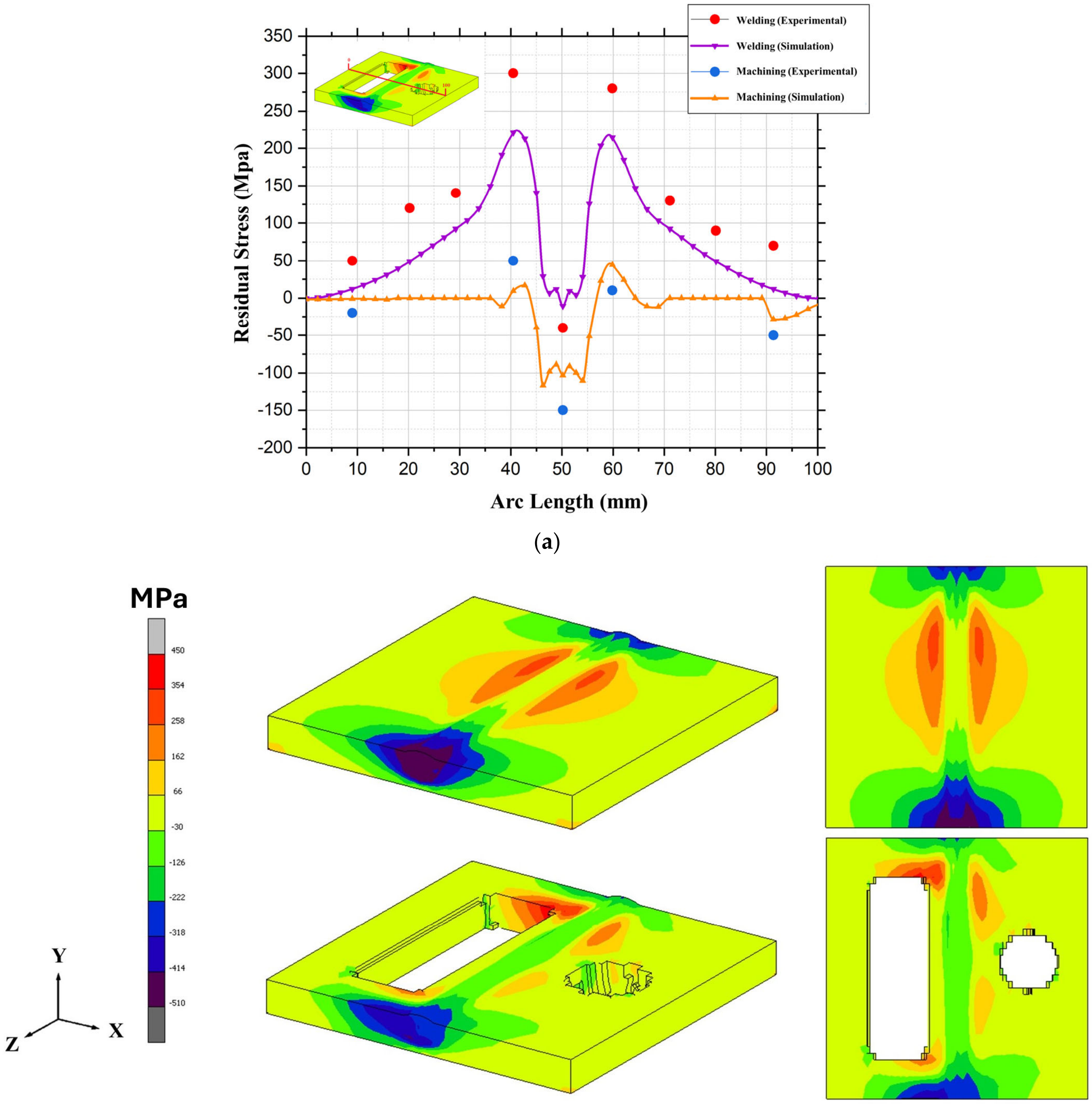

(**a**)

(**b**)

Figure 13. Residual stress distribution in welded and machined components in a 3D simulation: Transverse stresses (**a**) Graphical representation of residual stress in the x-direction (transverse), (**b**) Distribution of σ_{xx} post-welding and machining process.

Figure 15 illustrates the von Mises stress distribution to provide a comprehensive view of the stress state during machining. Von Mises stress is critical for evaluating material yielding under combined stress states, particularly in regions with complex stress interactions. The inclusion of von Mises stress aids in understanding potential failure mechanisms and complements the analysis of longitudinal and transverse stress distributions.

When comparing the different milling operations in Figures 14 and 15, it can be seen that although there is no significant stress loss along the weld seam as a result of cutting from the bottom surface of the part, there is an increase in negative stresses in areas outside the weld seam and HAZ. The holes drilled in the upper right and lower left of the part cause a diagonal change in the stress distribution of the part. In the third case, transverse pockets open over the weld seam of the part. Although these pockets dissipate the high residual stress values in the weld seam, the von Mises equivalent stress or total stress concentration increases due to the local stresses in this region.

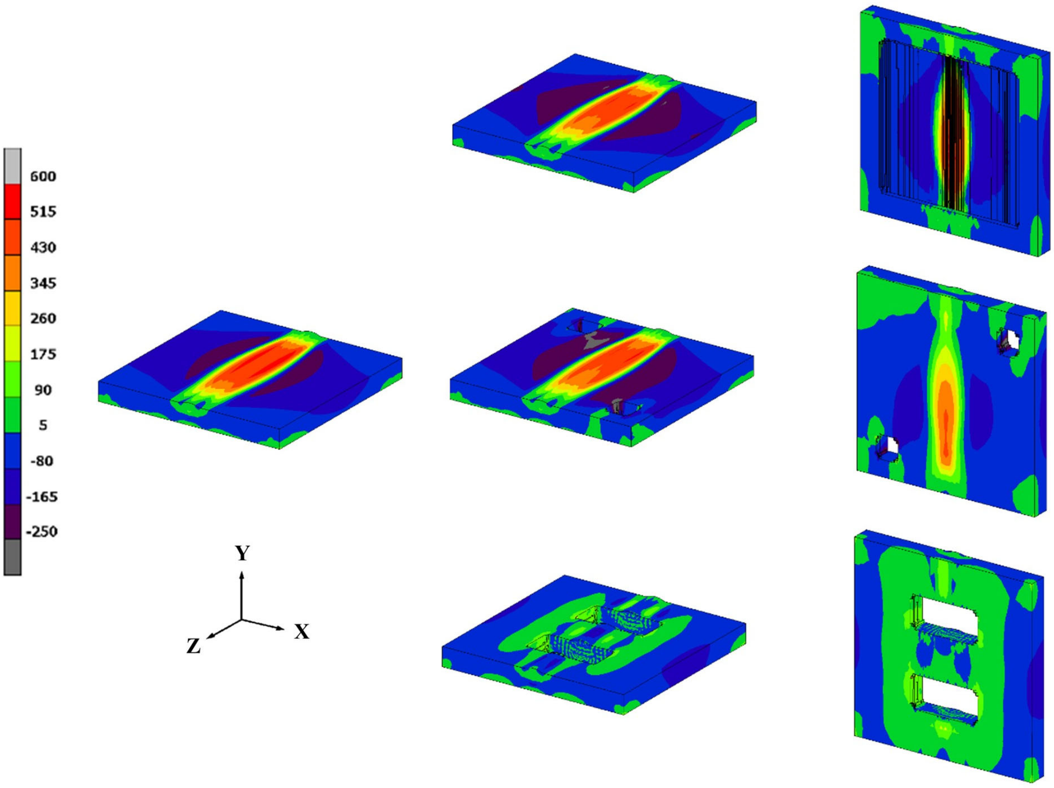

(**a**) (**b**) (**c**)

Figure 14. Longitudinal (z-direction) stress variations: (**a**) after welding, (**b**) normal view, and (**c**) bottom view of three different chip-removal conditions.

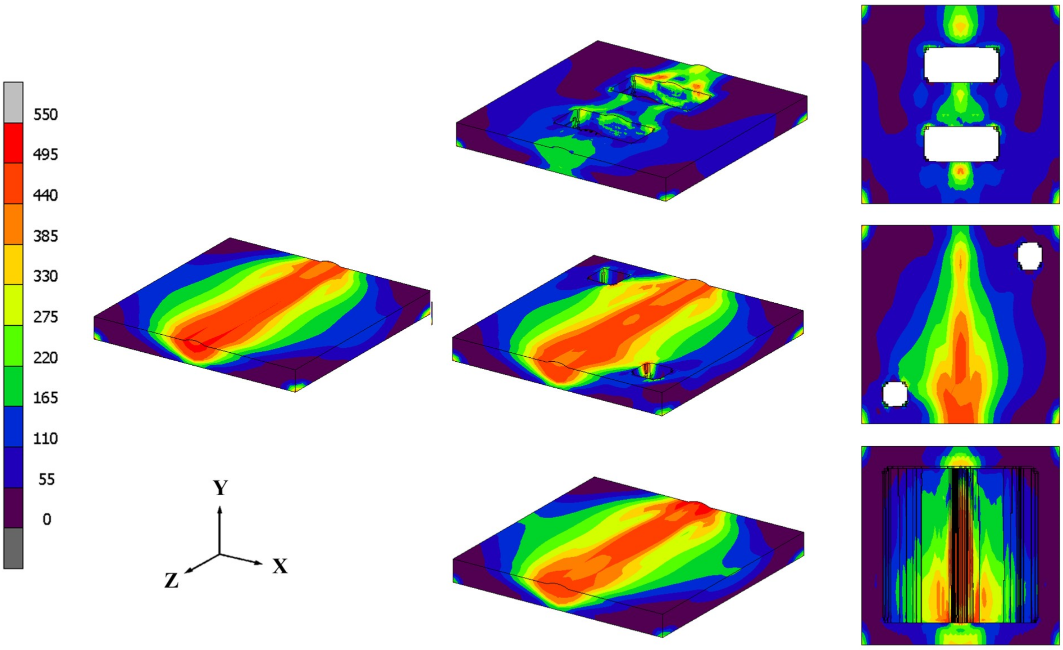

(**a**) (**b**) (**c**)

Figure 15. Equivalent von Mises stress variations: (**a**) after welding, (**b**) normal view, and (**c**) bottom view of three different chip-removal conditions.

Figure 16a shows the longitudinal stress (z-direction) along the weld section, Figure 16b shows the transverse stress (x-direction) of the same part, and Figure 16c shows the equivalent von Mises stress of the same part as a result of simulation of three-dimensional welding and milling processes. It has already been mentioned that the highest residual stress value after welding occurs along the weld seam. As seen below, the average longitudinal residual stress value along the cross section is as high as 500 MPa. However, after machining, this residual stress value hovers around 300 MPa on average. The transverse stress situation is similar. High temperature gradients during the welding process cause high residual stress values in the weld zone. Similarly, in all three shapes, the stress values after machining are considerably lower than after welding, but positive.

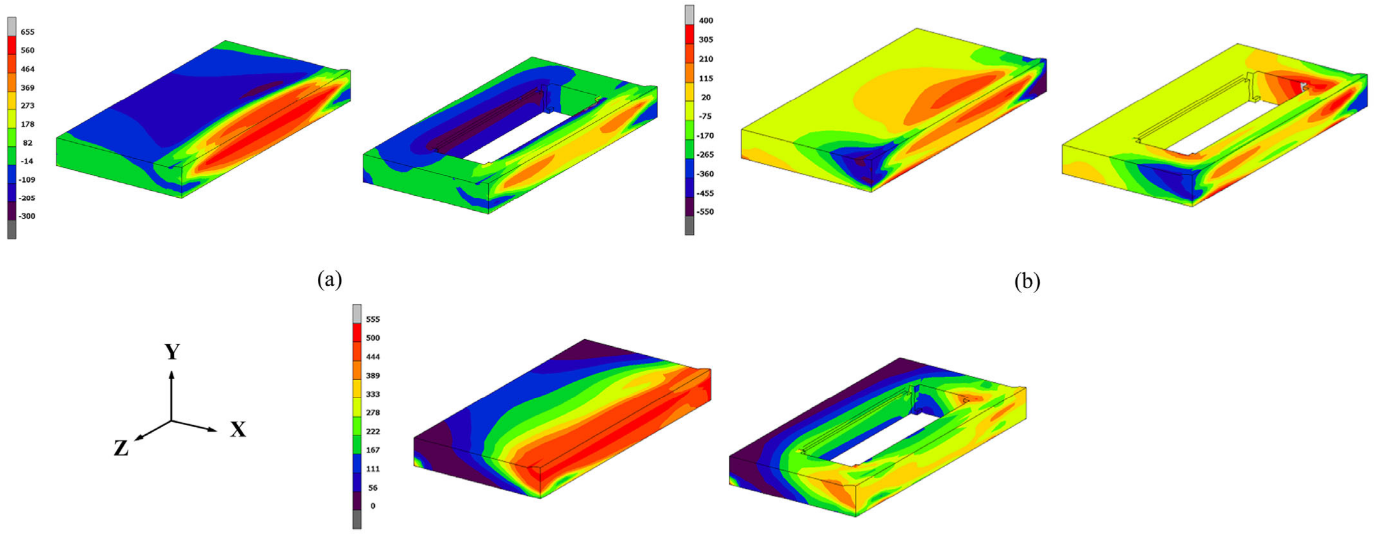

(a)

(b)

(c)

Figure 16. Overview of stress distribution after welding and machining, (**a**) Longitudinal (z-direction) stress, (**b**) Transverse stress (x-direction), (**c**) Equivalent von Mises stress.

The research conducted addresses the key problem identified in Section 1, which is the insufficient understanding of residual stress redistribution during sequential welding and machining processes. By developing and validating a 3D simulation model supported with experimental measurements, this study successfully demonstrates how residual stresses evolve when components undergo both welding and subsequent machining. The findings not only highlight the cumulative effects of these processes but also provide validated insights into stress redistribution, thereby bridging the gap in the literature regarding the impact of multi-step manufacturing on stress outcomes. This contributes to improved manufacturing reliability and optimized processing parameters, especially for applications requiring precise stress management, such as in aerospace and defense industries.

5. Conclusions

The present study aims to develop a sequential simulation method and the necessary infrastructure for this method and to investigate the accuracy of the method with experiments to investigate the numerical variation of residual stresses in any welded part with milling and cutting operations. The effects of mechanical tools are considered as simple stress-relieving operations, neglecting the importance of spontaneous residual stress. This hypothesis allows obtaining a simplified FE model to simulate the mechanical tooling or cutting process, which is quite sufficient to follow the modification of a pre-existing weld residual stress field. Based on the analysis results obtained, the main conclusions are summarized below:

1. 3D Model and Process Simulation: A 3D computational model was developed to predict residual stresses in butt-welded plates and their modification after milling. The stress from multi-pass welding was simulated and used as a pre-stress for subsequent milling.
2. Stress Redistribution: Local material removal acts as a stress-relief process. The experimental results confirm that the numerical model effectively predicts the stress modification caused by machining.
3. Impact of Material Removal: Minor local material removal results in only small variations in both longitudinal and transverse stresses, except near the tool contact areas.
4. Effect of Increased Material Removal: Greater material removal has a larger effect on transverse stress in the weld zone. Away from the weld, longitudinal stress is more affected.
5. Stress Changes with Material Removal Location: Stress redistribution depends on whether material is removed from the top or bottom of the plate, causing bending-like effects. These effects can be somewhat offset with different removal methods.
6. Longitudinal Stress Modification: After machining, tensile stress in the weld area turns compressive, with a high stress gradient near the weld axis. Cutting transverse joints reduces peak stress values but does not change the overall distribution.
7. Transverse Stress and Irregularities: Machining increases peak transverse stresses and introduces irregularities along the z-direction. The central region of specimens shows increased stress, while boundary areas compensate.
8. Experimental Verification: Experimental residual stress measurements largely validate the numerical model, especially for longitudinal stresses, while transverse stress measurements are more error-prone.

Based on the work performed in this study, the following suggestions are made for future work:

- More variations of the experimental setup are necessary to improve the validation of the finite element model. In particular, new experimental measurements are required at lines perpendicular and parallel to the weld at the beginning and end of the weld seam, at the bottom of the parts and inside the pipe if they are cylindrical, and at points around the machining areas.
- Future studies will explore additional machining configurations and refine mesh quality further to enhance simulation accuracy. Experimental setups will include stress measurements perpendicular to the weld seam and in deeper material layers to validate residual stress redistribution comprehensively.
- The clamping arrangement needs to be improved to avoid modeling stiffness in boundary conditions. Deformation measurements on the part are needed to investigate the relationship between residual stress and deformation.
- The results of the thesis show that it is of great importance to estimate the residual stresses for a defect or faulty weld section and machined areas on the part. The relationship between 2D analysis and 3D analysis for heat transfer and mechanical analysis should be further investigated. In the present thesis, there is good agreement between the 2D and 3D simulation results, but more variations in the welding and machining configuration need to be investigated to reach a general conclusion. Temperature-dependent material properties should be determined experimentally to reduce the uncertainties of FEA.

Author Contributions: Conceptualization, Y.C. and N.A.; methodology, I.C.; software, I.C.; validation, I.C., Y.C. and N.A.; investigation, I.C.; writing—original draft preparation, I.C., Y.C. and N.A.; writing—review and editing, Y.C. and N.A.; visualization, I.C.; supervision, Y.C. and N.A.; project administration, I.C.; funding acquisition, Y.C. All authors have read and agreed to the published version of the manuscript.

Funding: This research was funded by Trakya University Scientific Research Projects Unit, TUBAP Grant Number 2016/253.

Data Availability Statement: The original contributions presented in this study are included in the article. Further inquiries can be directed to the corresponding author.

Acknowledgments: The authors acknowledge financial support for this research by the Trakya University Scientific Research Projects Unit, TUBAP Grant Number 2016/253.

Conflicts of Interest: The authors declare no conflicts of interest.

References

1. Ball, D.L. An Update on the Impact of Forging Residual Stress in Airframe Component Design. *Mater. Perform. Charact.* **2018**, *7*, 827–861. [CrossRef]
2. Song, W.-Y.; Xu, C.-G.; Pan, Q.-X.; Li, P.-L.; Wang, L.; Yu, T. The Residual Stress and Deformation Control of TC4 Thin-Walled Outer Ring Components by Ultrasonic Regulation. *Machines* **2022**, *10*, 598. [CrossRef]
3. Ding, X.; Liang, X.; Chen, M.-T.; Hu, L. Study on CFRP-Strengthened Welded Steel Plates with Inclined Welds Considering Welding Residual Stress. *Materials* **2024**, *17*, 1804. [CrossRef]
4. Bertini, L.; Bucchi, F.; Frendo, F.; Moda, M.; Monelli, B.D. Residual Stress Prediction in Selective Laser Melting. *Int. J. Adv. Manuf. Technol.* **2019**, *105*, 609–636. [CrossRef]
5. Zach, T.F.; Dudescu, M.C. The Three-Dimensional Printing of Composites: A Review of the Finite Element/Finite Volume Modelling of the Process. *J. Compos. Sci.* **2024**, *8*, 146. [CrossRef]
6. Ma, K.; Goetz, R.; Srivatsa, S.K. Modeling of Residual Stress and Machining Distortion in Aerospace Components. In *Metals Process Simulation*; Furrer, D.U., Semiatin, S.L., Eds.; ASM International: Materials Park, OH, USA, 2010; Volume 22B, ISBN 978-1-62708-197-9.
7. Boillat-Newport, R.; Isanaka, S.P.; Kelley, J.; Liou, F. Heat Treatments for Minimization of Residual Stresses and Maximization of Tensile Strengths of Scalmalloy® Processed via Directed Energy Deposition. *Materials* **2024**, *17*, 1333. [CrossRef] [PubMed]
8. Tabatabaeian, A.; Ghasemi, A.R.; Shokrieh, M.M.; Marzbanrad, B.; Baraheni, M.; Fotouhi, M. Residual Stress in Engineering Materials: A Review. *Adv. Eng. Mater.* **2022**, *24*, 2100786. [CrossRef]
9. Residual Stress Development Due to High-Frequency Post Weld Impact Treatments for High-Strength Steels | TU Delft Repositories. Available online: https://repository.tudelft.nl/islandora/object/uuid:2029863f-4967-4796-ba4f-199dca8c7212?collection=research (accessed on 7 April 2024).
10. Manai, A.; von Bock und Polach, R.U.F.; Al-Emrani, M. A Probabilistic Study of Welding Residual Stresses Distribution and Their Contribution to the Fatigue Life. *Eng. Fail. Anal.* **2020**, *118*, 104787. [CrossRef]
11. Jaisawal, R.; Gaur, V.; Ahmed, S. On Improved Fatigue Properties of Aluminum Alloy 5086 Weld Joints. *Int. J. Fatigue* **2023**, *174*, 107712. [CrossRef]
12. Marques, E.S.V.; Silva, F.J.G.; Pereira, A.B. Comparison of Finite Element Methods in Fusion Welding Processes—A Review. *Metals* **2020**, *10*, 75. [CrossRef]
13. Outeiro, J.C. 11—Residual Stresses in Machining. In *Mechanics of Materials in Modern Manufacturing Methods and Processing Techniques*; Silberschmidt, V.V., Ed.; Elsevier: Amsterdam, The Netherlands, 2020; pp. 297–360. ISBN 978-0-12-818232-1.
14. Gurmesa, F.D.; Lemu, H.G. Literature Review on Thermomechanical Modelling and Analysis of Residual Stress Effects in Wire Arc Additive Manufacturing. *Metals* **2023**, *13*, 526. [CrossRef]
15. Chintapalli, R.K.; Mestra Rodriguez, A.; Garcia Marro, F.; Anglada, M. Effect of Sandblasting and Residual Stress on Strength of Zirconia for Restorative Dentistry Applications. *J. Mech. Behav. Biomed. Mater.* **2014**, *29*, 126–137. [CrossRef]
16. Thadsoongnoen, K.; Hasap, A.; Noraphaiphipaksa, N.; Kanchanomai, C. Numerical Investigation of Residual Stress Formation Mechanisms in Flash-Butt Welded Rail. *Metals* **2023**, *13*, 1359. [CrossRef]
17. Mukherjee, T.; Zhang, W.; DebRoy, T. An Improved Prediction of Residual Stresses and Distortion in Additive Manufacturing. *Comput. Mater. Sci.* **2017**, *126*, 360–372. [CrossRef]
18. Jagarinec, D.; Gubeljak, N. Effect of Residual Stresses on the Fatigue Stress Range of a Pre-Deformed Stainless Steel AISI 316L Exposed to Combined Loading. *Metals* **2024**, *14*, 1084. [CrossRef]
19. Kaimkuriya, A.; Sethuraman, B.; Gupta, M. Effect of Physical Parameters on Fatigue Life of Materials and Alloys: A Critical Review. *Technologies* **2024**, *12*, 100. [CrossRef]
20. Liu, F.; Tao, C.; Dong, Z.; Jiang, K.; Zhou, S.; Zhang, Z.; Shen, C. Prediction of Welding Residual Stress and Deformation in Electro-Gas Welding Using Artificial Neural Network. *Mater. Today Commun.* **2021**, *29*, 102786. [CrossRef]
21. Li, Z.; Guo, Y.; Dong, H.; Yuan, F.; Wu, H.; Xu, H.; Ke, Y. Numerical Prediction and Control of Deformation and Residual Stress in Double-Sided Arc Welding of Large Pressure Hull. *Measurement* **2025**, *242*, 115955. [CrossRef]
22. Ahmad, A.S.; Wu, Y.; Gong, H.; Nie, L. Finite Element Prediction of Residual Stress and Deformation Induced by Double-Pass TIG Welding of Al 2219 Plate. *Materials* **2019**, *12*, 2251. [CrossRef]
23. Friederich, J.; Lazarova-Molnar, S. Reliability Assessment of Manufacturing Systems: A Comprehensive Overview, Challenges and Opportunities. *J. Manuf. Syst.* **2024**, *72*, 38–58. [CrossRef]
24. Yu, C.; Pan, J.; Han, J.; Ma, J.; Zhang, W. Numerical Simulation Study on Welding Process of Upper Frame of Hydropower Unit. *Appl. Sci.* **2024**, *14*, 4268. [CrossRef]

25. Chen, B.-Q.; Liu, K.; Xu, S. Recent Advances in Aluminum Welding for Marine Structures. *J. Mar. Sci. Eng.* **2024**, *12*, 1539. [CrossRef]
26. Xu, W.; Li, H.; Song, Z.; Meng, C. An Assessment of the Residual Stress of Pipelines Subjected to Localized Large Deformations. *J. Mar. Sci. Eng.* **2024**, *12*, 1789. [CrossRef]
27. Jang, H.-L.; Ryu, H.; Kang, S. A Study on the Effects of Welding Deformation According to Weld Sequence in Overlay-Welded Structures. *Metals* **2024**, *14*, 684. [CrossRef]
28. Tran, H.-S.; Tchuindjang, J.T.; Paydas, H.; Mertens, A.; Jardin, R.T.; Duchêne, L.; Carrus, R.; Lecomte-Beckers, J.; Habraken, A.M. 3D Thermal Finite Element Analysis of Laser Cladding Processed Ti-6Al-4V Part with Microstructural Correlations. *Mater. Des.* **2017**, *128*, 130–142. [CrossRef]
29. Hekmatjou, H.; Zeng, Z.; Shen, J.; Oliveira, J.P.; Naffakh-Moosavy, H. A Comparative Study of Analytical Rosenthal, Finite Element, and Experimental Approaches in Laser Welding of AA5456 Alloy. *Metals* **2020**, *10*, 436. [CrossRef]
30. Jin, Z.; Dong, P.; Song, S. A Physically Consistent 2D Residual Stress Model for Approximating 3D Effects in Welding. *Int. J. Press. Vessel. Pip.* **2024**, *210*, 105244. [CrossRef]
31. Gu, L.; Hong, J.; Ma, N. Analysis and Simplified Model Calculation of Residual Stress in U-Rib Welding of Steel Bridge Deck. *Adv. Mech. Eng.* **2024**, *16*, 16878132241266457. [CrossRef]
32. Sarmast, A.; Schubnell, J.; Farajian, M. Finite Element Simulation of Multi-Layer Repair Welding and Experimental Investigation of the Residual Stress Fields in Steel Welded Components. *Weld. World* **2022**, *66*, 1275–1290. [CrossRef]
33. Asano, W.; Katsuyama, J.; Onizawa, K.; Mochizuki, M.; Toyoda, M. Effect of Surface-Machining and Butt-Welding on Residual Stress and Hardness of Type 316L Stainless Steel Pipes. In Proceedings of the ASME 2008 Pressure Vessels and Piping Conference, Chicago, IL, USA, 27–31 July 2008; pp. 451–458.
34. Dattoma, V.; De Giorgi, M.; Nobile, R. On the Evolution of Welding Residual Stress after Milling and Cutting Machining. *Comput. Struct.* **2006**, *84*, 1965–1976. [CrossRef]
35. Ihara, R.; Katsuyama, J.; Onizawa, K.; Hashimoto, T.; Mikami, Y.; Mochizuki, M. Prediction of Residual Stress Distributions Due to Surface Machining and Welding and Crack Growth Simulation under Residual Stress Distribution. *Nucl. Eng. Des.* **2011**, *241*, 1335–1344. [CrossRef]
36. Liu, C.; Zhang, J. Numerical and Experimental Investigations on the Modification of As-Welded Residual Stress after Local Material Removal. *J. Strain Anal. Eng. Des.* **2011**, *46*, 444–455. [CrossRef]
37. Wang, Z.; Gong, M.; Zhou, L.; Gao, M. A Review of Numerical Simulation of Laser–Arc Hybrid Welding. *Materials* **2023**, *16*, 3561. [CrossRef] [PubMed]
38. Hu, S.; Li, F.; Zuo, P. Numerical Simulation of Laser Transmission Welding—A Review on Temperature Field, Stress Field, Melt Flow Field, and Thermal Degradation. *Polymers* **2023**, *15*, 2125. [CrossRef] [PubMed]
39. Sun, F.; Fu, G.; Huo, D. Computational and Experimental Analysis of Surface Residual Stresses in Polymers via Micro-Milling. *Polymers* **2024**, *16*, 273. [CrossRef]
40. Wang, J.; Kong, B.; Wei, S.; Zang, J.; Li, A. Simulation Study on Residual Stress Distribution of Machined Surface Layer in Two-Step Cutting of Titanium Alloy. *Materials* **2024**, *17*, 4283. [CrossRef] [PubMed]
41. Natesan, E.; Ahlström, J.; Eriksson, S.; Persson, C. Effects of Temperature on the Evolution of Yield Surface and Stress Asymmetry in A356–T7 Cast Aluminium Alloy. *Materials* **2021**, *14*, 7898. [CrossRef]
42. Feli, S.; Aalami Aaleagha, M.E.; Foroutan, M.; Borzabadi Farahani, E. Finite Element Simulation of Welding Sequences Effect on Residual Stresses in Multipass Butt-Welded Stainless Steel Pipes. *J. Press. Vessel Technol.* **2011**, *134*, 4571. [CrossRef]
43. Gomes, D.d.A.; Castro, J.A.; Xavier, C.R.; Lima, C.A.C. Analysis of Residual Stress by the Hole-Drilling Method and Hardness in Dissimilar Joints of Austenitic Stainless Steel AISI 316L and Inconel 718 Alloy by Autogenous GTAW Process. *Mater. Res.* **2019**, *22*, e20180844. [CrossRef]
44. Goldak, J.; Chakravarti, A.; Bibby, M. A New Finite Element Model for Welding Heat Sources. *Metall. Trans. B* **1984**, *15*, 299–305. [CrossRef]
45. Ghafouri, M.; Ahola, A.; Ahn, J.; Björk, T. Numerical and Experimental Investigations on the Welding Residual Stresses and Distortions of the Short Fillet Welds in High Strength Steel Plates. *Eng. Struct.* **2022**, *260*, 114269. [CrossRef]